

See discussions, stats, and author profiles for this publication at: <https://www.researchgate.net/publication/6341537>

# Temperature-Dependent Mechanistic Transition for Photoinduced Electron Transfer Modulated by Excited-State Vibrational Relaxation Dynamics †

ARTICLE *in* THE JOURNAL OF PHYSICAL CHEMISTRY B · JULY 2007

Impact Factor: 3.3 · DOI: 10.1021/jp070414f · Source: PubMed

---

CITATIONS

16

---

READS

9

3 AUTHORS, INCLUDING:



**Youn K. Kang**

Sangmyung University

34 PUBLICATIONS 619 CITATIONS

SEE PROFILE

# Temperature-Dependent Mechanistic Transition for Photoinduced Electron Transfer Modulated by Excited-State Vibrational Relaxation Dynamics<sup>†</sup>

Youn K. Kang, Timothy V. Duncan, and Michael J. Therien\*

Department of Chemistry, University of Pennsylvania, Philadelphia, Pennsylvania 19104-6323

Received: January 17, 2007; In Final Form: March 8, 2007

The electron transfer (ET) dynamics of an unusually rigid  $\pi$ -stacked (porphinato)zinc(II)-spacer-quinone (PZn-Q) system, [5-[8'-(4''-[8'''-(2''''-5''''-benzoquinonyl)-1'''-naphthyl]-1''-phenyl)-1'-naphthyl]-10,20-diphenylporphinato]zinc(II) (**2a-Zn**), in which sub-van der Waals interplanar distances separate juxtaposed porphyrin, aromatic bridge, and quinonyl components of this assembly, have been measured by ultrafast pump–probe transient absorption spectroscopy over a 80–320 K temperature range in 2-methyl tetrahydrofuran (2-MTHF) solvent. Analyses of the photoinduced charge-separation (CS) rate data are presented within the context of several different theoretical frameworks. Experiments show that at higher temperatures the initially prepared **2a-Zn** vibrationally excited  $S_1$  state relaxes on an ultrafast time scale, and ET is observed exclusively from the equilibrated lowest-energy  $S_1$  state ( $CS_1$ ). As the temperature decreases, production of the photoinduced charge-separated state directly from the vibrationally unrelaxed  $S_1$  state ( $CS_2$ ) becomes competitive with the vibrational relaxation time scale. At the lowest experimentally interrogated temperature ( $\sim 80$  K),  $CS_2$  defines the dominant ET pathway. ET from the vibrationally unrelaxed  $S_1$  state is temperature-independent and manifests a subpicosecond time constant; in contrast, the  $CS_1$  rate constant is temperature-dependent, exhibiting time constants ranging from  $4 \times 10^{10} \text{ s}^{-1}$  to  $4 \times 10^{11} \text{ s}^{-1}$  and is correlated strongly with the temperature-dependent solvent dielectric relaxation time scale over a significant temperature domain. Respective electronic coupling matrix elements for each of these photoinduced  $CS_1$  and  $CS_2$  pathways were determined to be  $\sim 50$  and  $\sim 100 \text{ cm}^{-1}$ . This work not only documents a rare, if not unique, example of a system where temperature-dependent photoinduced charge-separation (CS) dynamics from vibrationally relaxed and unrelaxed  $S_1$  states can be differentiated, but also demonstrates a temperature-dependent mechanistic transition of photoinduced CS from the nonadiabatic to the solvent-controlled adiabatic regime, followed by a second temperature-dependent mechanistic evolution where CS becomes decoupled from solvent dynamics and is determined by the extent to which the vibrationally unrelaxed  $S_1$  state is populated.

## Introduction

Variable-temperature experiments provide considerable mechanistic insight into intramolecular electron transfer (ET) reactions.<sup>1–23</sup> Depending on the characteristic features of the system, which include interactions with solvent, temperature dependence of the ET rate constants can be rationalized within a variety of mechanistic constructs. For example, nonadiabatic ET events that occur on a time scale much slower than that of solvent dynamics can be modeled well by modern ET theory.<sup>24–30</sup> Likewise, both temperature-dependent<sup>9,11,13,18,31</sup> and temperature-independent<sup>8,12,17,19</sup> ET have been interpreted under these theoretical frameworks.

When the ET dynamics are coupled to solvent motion, the extent to which ET rate constants are temperature-dependent cannot be predicted easily. For instance, although theories predict the longitudinal solvent relaxation time ( $\tau_L^{-1}$ ) as an upper limit to the ET rate constants,<sup>32–34</sup> there have been a number of reports that clearly demonstrate ET rate constants much larger than  $\tau_L^{-1}$ .<sup>35–43</sup> Although the nature of this discrepancy is not always clear, mechanistic insight can be attained if the system under study exhibits a clear, observable transition from the solvent-controlled regime to a regime where ET rate constants exceed  $\tau_L^{-1}$ . Examples of such systems are es-

entially limited to those reported by Kosower and co-workers,<sup>44,45</sup> which were interrogated prior to the advent of ultrafast pump–probe transient optical methods.

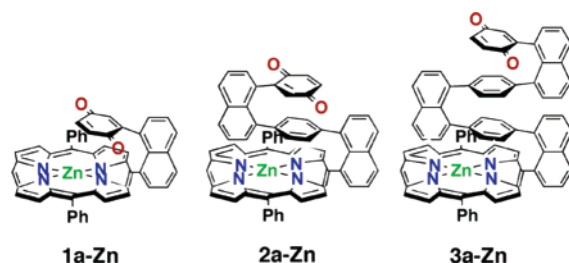
We reported recently the synthesis of a series of rigid,  $\pi$ -stacked, compressed porphyrin–bridge–quinone systems (**1a-Zn**, **2a-Zn**, and **3a-Zn**, Chart 1) that feature cofacial spacer, quinone, and (porphinato)zinc(II) units.<sup>46,47</sup> In these species, a 1,8-naphthyl pillaring motif imposes sub-van der Waals interplanar separation between juxtaposed porphyrin, aromatic bridge, and quinonyl components, which limits the range of allowed relative vertical displacement and lateral motion in these species. The room-temperature photoinduced ET and thermal charge-recombination kinetics for this family of donor–spacer–acceptor (D–Sp–A) systems has been reported,<sup>47</sup> and a soft distance dependence of the ET rate constants was noted for both the charge-separation (CS) and charge-recombination (CR) processes. Theoretical studies<sup>48</sup> showed that for **2a-Zn** and **3a-Zn** the phenyl spacer units dominate the mediation of D–A electronic coupling, and that the relatively large D–A electronic interaction manifest by these systems has its genesis from the significant  $\pi$  compression of the D, Sp, and A units.

Given the unique rigid cofacial structure of this family of electron-transfer assemblies, and the facts that the D, Sp, and A units of those structures possess restricted vibrational degrees of freedom and exhibit attenuated interactions with the solvent bath, temperature-dependent charge-separation and charge-recom-

<sup>†</sup> Part of the special issue “Norman Sutin Festschrift”.

\* Corresponding author. E-mail: therien@sas.upenn.edu.

## CHART 1: Structure Block



bination dynamics were probed in a variety of solvent environments. In this first paper, we focus on a structure of intermediate size, **2a-Zn**, report the unusual dependence of photoinduced intramolecular ET on temperature in 2-methyl-tetrahydrofuran (2-MTHF) solvent, and analyze the experimental ET rate data within the context of several different theoretical frameworks.

## Experimental Section

The synthesis of **2a-Zn** has been reported previously.<sup>46,47</sup> Samples were purified by column chromatography (CHCl<sub>3</sub>, Silica Gel 60, 230–400 mesh, EM Science) prior to the transient absorption measurements. 2-Methyltetrahydrofuran (2-MTHF, Aldrich) was distilled over K/benzoylbiphenyl and degassed via three freeze–pump–thaw cycles. The solvent was transferred via cannula under N<sub>2</sub> into a Schlenk flask that contained the sample immediately before the measurement. The concentrations of sample solutions were fixed by adjusting the optical density at the excitation wavelength to ~0.5 O.D. The prepared sample solution was then transferred carefully into a quartz cell (3 mm path length, NSG Precision Cells), which was then harnessed in the sample holder of the cryostat. The cryostat (Optistat DN, Oxford Instruments) controls the sample temperature to within ±0.1 K.

Transient absorption spectra were obtained via standard pump–probe methods, using a spectrometry system that has been described previously.<sup>49</sup> In brief, optical pulses (≥120 fs) centered at 775 nm, are generated using a Ti:Sapphire laser (Clark-MXR, CPA-2001), which consists of a regenerative amplifier seeded by a mode-locked fiber oscillator. Optical parametric amplifiers (near-IR and visible OPAs, Clark-MXR) generate excitation pulses tunable in wavelength from the UV through the near-IR region. The pump beam, chopped at half the laser repetition rate (~500 Hz), is passed through an optical delay line. The pump beam intensity is monitored using a silicon photodiode. A fraction of the output from the regenerative amplifier is focused into a 2 mm c-cut sapphire plate to generate a white-light continuum, which is used as the probe beam. The polarization of the pump and probe beams is controlled by a half-wave plate and an appropriate polarizer (probe – thin film, pump–Rochor prism). The pump beam is focused into the sample cell with an  $f = 40$  cm lens, while the probe beam is focused with an  $f = 10$  cm lens. After passing through the sample, the probe light is focused onto the entrance slit of the computer-controlled image spectrometer (SpectraPro-150, Acton Research Corporation). A CCD array detector (Roper Scientific, 1024 × 128 elements), interfaced to the spectrometer, records the spectrum of the probe light from the UV (~370 nm) to the near-IR (~1100 nm), providing spectral resolution better than 0.5 nm. To provide shot-by-shot detection at a 1 kHz repetition rate, the entrance slit of the image spectrometer is optically masked to shield the upper bins of the CCD. Thirty-two data points are binned for each wavelength, with the resulting spectrum transferred to the computer. Pairs of consecu-

tive spectra are measured with ( $I_{\text{on}}(\lambda)$ ) and without ( $I_{\text{off}}(\lambda)$ ) optical pumping to determine the difference spectrum,  $\Delta A = \log(I_{\text{off}}(\lambda)/I_{\text{on}}(\lambda))$ . All transient spectra reported represent averages obtained over 4–10 scans with each scan consisting of 150–250 points. At temperatures below the solvent glassing temperature, the sample position was adjusted following each scan to prevent photobleaching.

The delay line utilizes three computer-controlled delay stages. Short time delays are effected with Nanomover stages (Melles Griot), whereas longer delay times (up to 8.5 ns) are achieved using a Compumotor-6000 (Parker). The baseline noise level in these transient absorption experiments corresponds to ~0.1 mOD per second of signal accumulation. The time resolution is probe-wavelength-dependent; in these experiments, the FWHM of the instrument response function (IRF) varied from 140 to 200 fs (e.g., at 680 nm, the IRF was  $150 \pm 6$  fs). The sample pump energy was ~300 nJ; the spot size diameter was 0.3 mm.

**Theoretical Background.** The classical expression for the rate constant of a nonadiabatic electron transfer can be written as

$$k_{\text{ET}} = \frac{2\pi}{\hbar} \frac{V_{\text{el}}^2}{\sqrt{4\pi\lambda_{\text{T}} k_{\text{B}} T}} \exp\left(-\frac{(\Delta G + \lambda_{\text{T}})^2}{4\lambda_{\text{T}} k_{\text{B}} T}\right) \quad (1)$$

where  $k_{\text{B}}$  and  $\hbar$  are the respective Boltzmann and Planck constants,  $V_{\text{el}}$  is the electronic coupling matrix element,  $T$  is the temperature,  $\Delta G$  is the free energy difference between the product and reactant states, and  $\lambda_{\text{T}}$  is the total reorganization energy, which is the sum of an inner sphere term,  $\lambda_{\text{i}}$ , and an outer sphere term,  $\lambda_{\text{o}}$ .<sup>24–26</sup>

$$\lambda_{\text{T}} = \lambda_{\text{i}} + \lambda_{\text{o}} \quad (2)$$

Equation 1 can be interpreted as a classical transition-state rate equation. Because the activation energy and the preexponential factor can be extracted from the Arrhenius equation, eq 1 can be rewritten (eq 3).<sup>9,11,13,18</sup>

$$\ln(k_{\text{ET}}\sqrt{T}) = \ln\left(\frac{2\pi}{\hbar} \frac{V_{\text{el}}^2}{\sqrt{4\pi\lambda_{\text{T}} k_{\text{B}} T}}\right) - \frac{(\Delta G + \lambda_{\text{T}})^2}{4\lambda_{\text{T}} k_{\text{B}} T} \frac{1}{T} \quad (3)$$

An important caveat of such an ET analysis is that  $\Delta G$  (or  $\lambda$ ) should be constant within the temperature window studied. In most cases, however,  $\Delta G$  (or  $\lambda$ ) varies with temperature. This can be understood, in part, by considering the Weller equation<sup>50</sup> (eq 4) and Marcus' expression for the outer-sphere reorganization energy (eq 5).<sup>24,51</sup>

$$\Delta G_{\text{CS}} = e(E_{\text{ox}} - E_{\text{red}}) - E_{00} - \frac{e^2}{4\pi\epsilon_0\epsilon_{\text{S}}R_{\text{DA}}} + \frac{e^2}{4\pi\epsilon_0}\left(\frac{1}{\epsilon_{\text{S}}} - \frac{1}{\epsilon_{\text{S}}^{\text{ref}}}\right)\left(\frac{1}{2R_{\text{D}}} + \frac{1}{2R_{\text{A}}}\right) \quad (4)$$

$$\lambda_{\text{S}} = \frac{e^2}{4\pi\epsilon_0}\left(\frac{1}{\epsilon_{\text{op}}} - \frac{1}{\epsilon_{\text{S}}}\right)\left(\frac{1}{2R_{\text{D}}} + \frac{1}{2R_{\text{A}}} - \frac{1}{R_{\text{DA}}}\right) \quad (5)$$

Here  $E_{\text{ox}}$  and  $E_{\text{red}}$  are the respective donor (D) and acceptor (A) redox potentials,  $E_{00}$  is the zero energy of the excited molecule,  $R_{\text{DA}}$  is the D–A distance,  $R_{\text{D}}$  and  $R_{\text{A}}$  are the donor and acceptor ionic radii,  $\epsilon_{\text{S}}$  and  $\epsilon_{\text{op}}$  are the respective static and optical dielectric constants of the solvent, and  $\epsilon_{\text{S}}^{\text{ref}}$  is the static dielectric constant of the solvent in which redox potentials were

measured. Among the parameters that control  $\Delta G$  and  $\lambda$ , the temperature dependence of both the static and the optical dielectric constants are often quite pronounced; for this reason, extracting electronic coupling or energetic parameters from the fitting of experimental data with eq 3 can only be carried out with confidence over a narrow temperature range. Many reports examining the temperature dependence of ET have analyzed data under these constraints.<sup>9,11,13,18,31</sup>

This approach, however, cannot reconcile the situation where a high-frequency, intramolecular vibrational mode that undergoes a significant displacement is coupled to ET. Nuclear tunneling becomes important in this case, and incorporating a quantum-mechanical, high-frequency intramolecular vibrational mode becomes necessary to describe the ET dynamics properly. The semiclassical rate expression considers a single reactant state free-energy surface that couples to those of multiple high-frequency vibrational modes of the product state (eqs 6 and 7).<sup>27–30</sup>

$$k_{\text{ET}} = \frac{2\pi}{\hbar} \frac{V_{\text{el}}^2}{\sqrt{4\pi\lambda_{\text{cl}}k_{\text{B}}T}} \exp(-S_{\text{c}}) \sum_{m=0}^{\infty} \frac{S_{\text{c}}^m}{m!} \exp\left(-\frac{(\Delta G + \lambda_{\text{cl}} + m\hbar\langle\omega\rangle)^2}{4\lambda_{\text{cl}}k_{\text{B}}T}\right) \quad (6)$$

$$S_{\text{c}} = \frac{\lambda_i}{\hbar\langle\omega\rangle} \quad (7)$$

Here  $\langle\omega\rangle$  is the average frequency of the high-frequency vibrational modes in the reactant state,  $S_{\text{c}}$  is the Huang–Rhys factor (eq 7),  $\lambda_i$  is the nuclear reorganization energy related to the quantum-mechanical, high-frequency intramolecular vibrational modes that are coupled to the ET reaction,  $\lambda_{\text{cl}}$  is the reorganization energy of classical modes that include solvent polarization and low-frequency intramolecular vibration, and  $m$  is the high-frequency vibrational quantum number. Other parameters are the same as those described for eq 1. In the high-temperature limit ( $k_{\text{B}}T \gg \hbar\omega$ ), this expression also predicts an Arrhenius-type temperature dependence of ET rate constants if the ET energetics place the reaction in the Marcus normal region. In the low-temperature limit ( $k_{\text{B}}T \ll \hbar\omega$ ), however, the Poisson-type function ( $k_{\text{ET}} \propto \exp(-S_{\text{c}}S_{\text{c}}^m/n!)$ ) prevails and the temperature dependence of ET reaction rate constants becomes very weak. It is important to note that both classical and semiclassical models predict a weak temperature dependence of the ET rate constant for the case where the energetics restrict the system to the Marcus activationless or inverted region, even in the high-temperature limit. Note that nuclear tunneling plays an important role in the inverted region and can cause the temperature dependence of the ET rate constants plotted as a function of temperature to exhibit a negative slope when the temperature-dependent solvent reorganization energy and reaction free energy are taken into account.<sup>12</sup>

When the ET dynamics are coupled to the solvent dynamics, the temperature-dependent description of the ET rate constant requires a more sophisticated approach. Dynamical solvent effects are usually discussed from a collisional or dielectric point of view;<sup>52</sup> the latter has attracted much attention in connection with the ET reaction. The extent to which solvent dynamics influence ET reactions depends on the nature of the solute–solvent interaction, which is electrostatic in origin. Because an intramolecular ET reaction is accompanied by a drastic change in molecular polarity, an ET reaction is more likely to be coupled

to the motion of polar solvent molecules.<sup>7,53–56</sup> Theoretical treatment of this type of ET reaction is based on Zusman's stochastic Liouville equation approach; following experimental verification, this mechanism has been termed as the solvent-controlled adiabatic reaction.<sup>32–34,57–67</sup> One important issue regarding this ET mechanism is the time-scale relation between the solvent dynamics and the ET event. When the ET reaction time scale is much slower than that of solvent dynamics, the ET rate constant is governed mainly by the electronic tunneling probability at a given driving force, and is thus nonadiabatic. Only when the ET rate constant is comparable to or faster than that for solvent dynamics does the solvent-controlled adiabatic mechanism prevail; only in this case does the time scale at which the reactant system approaches the transition state become rate-determined by solvent friction. The transition from a nonadiabatic to a solvent-controlled adiabatic ET reaction mechanism is thus possible when the time scale of the ET reaction has relatively weak temperature dependence and coincides with that of solvent dynamics.<sup>21,68–71</sup>

It is worth mentioning that most theories predict  $\tau_{\text{L}}^{-1}$  as an upper limit for the ET rate constant in the solvent-controlled adiabatic regime. Some experimental results, however, have clearly showed an ET rate faster than  $\tau_{\text{L}}^{-1}$ .<sup>35–43</sup> Two extremes of different experimental results,  $k_{\text{ET}} \leq \tau_{\text{L}}^{-1}$  and  $k_{\text{ET}} > \tau_{\text{L}}^{-1}$ , have been interpreted in light of the Sumi–Marcus two-dimensional free-energy surface model, which considers an intramolecular vibrational degree of freedom ( $q$ ) and a classical solvent degree of freedom ( $X$ ).<sup>72</sup> The case where the ET rate constant exceeds  $\tau_{\text{L}}^{-1}$  can be categorized as belonging to the “nondiffusing limit”; here, the reactant-to-product transition proceeds so rapidly at the initial values of the slow coordinate  $X$  that the distribution of  $X$  is not restored by diffusion in the course of the reaction, causing the reaction rate to no longer depend on the relaxation time  $\tau_{\text{L}}$  of the  $X$  coordinate. This model was later expanded to include a quantum-mechanical nuclear degree of freedom by Barbara and co-workers;<sup>35,73,74</sup> we adopt this Sumi–Marcus–Barbara (SMB, eq 11) model for the data analysis presented in this paper. Note that this model, as well as those discussed previously, assumes thermal equilibration in the donor manifold.

$$\tau_{\text{SMB,a}} = \int_0^{\infty} Q(t) dt \quad (8)$$

$$\tau_{\text{SMB,b}} = \frac{\int_0^{\infty} tQ(t) dt}{\int_0^{\infty} Q(t) dt} \quad (9)$$

$$Q(t) = \exp\left\{-\int_0^t k_{\text{ET}}(t) dt\right\} \quad (10)$$

$$k_{\text{ET}}(t) = \frac{2\pi}{\hbar} \frac{V_{\text{el}}^2}{\sqrt{4\pi\lambda_{\text{cl,vib}}k_{\text{B}}T}} \exp(-S_{\text{c}}) \sum_{m=0}^{\infty} \frac{S_{\text{c}}^m}{m!} \exp\left[-\frac{(\Delta G + \lambda_{\text{cl,vib}} + \{1 - 2X(t)\}\lambda_{\text{s}} + m\hbar\langle\omega\rangle)^2}{4\lambda_{\text{s}}k_{\text{B}}T}\right] \quad (11)$$

Here,  $\lambda_{\text{cl,vib}}$  is the vibrational reorganization energy due to solvent molecules and  $\tau_{\text{s}}$  is the solvation time;  $Q(t)$  denotes the survival probability of the initially prepared population by laser pulse excitation [ $Q(0) = 1$  and  $Q(\infty) = 0$ ]. Average survival times of  $\tau_{\text{SMB,a}}$  and  $\tau_{\text{SMB,b}}$  emphasize the fast and slow decaying



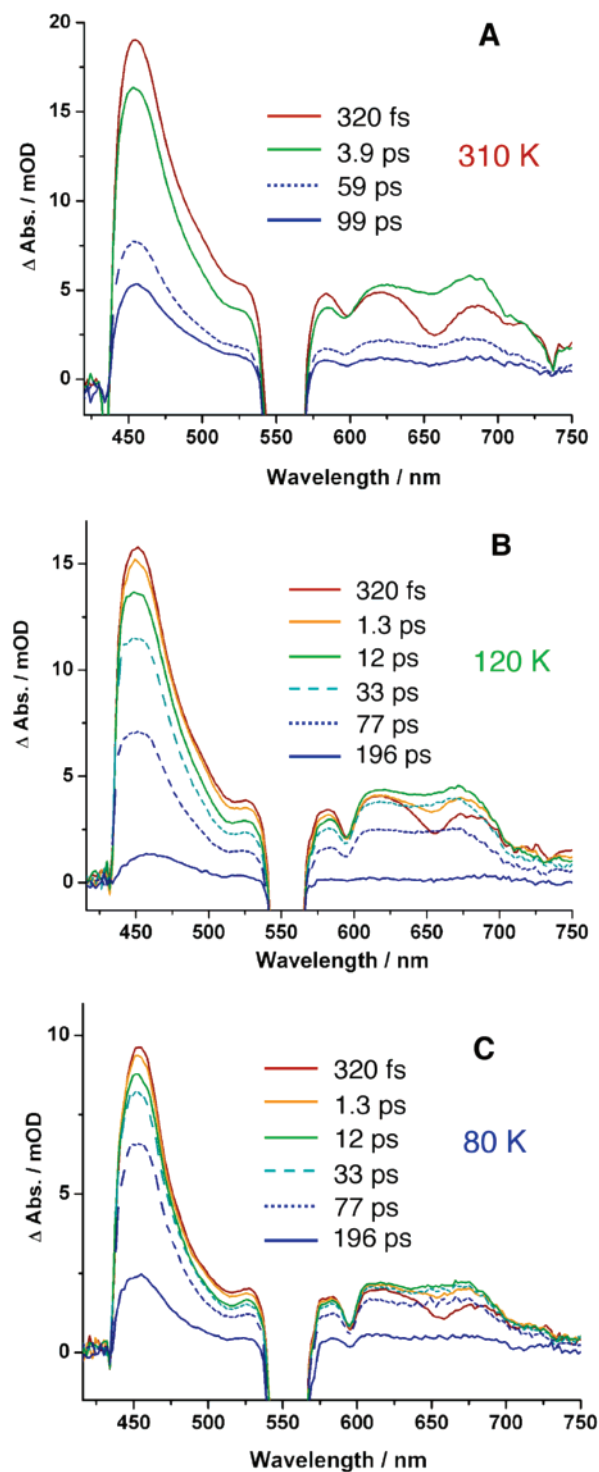


**Figure 1.** 2a-Zn transient absorption spectra recorded at (A) 310, (B) 120, and (C) 80 K. Time delays are shown as insets. Experimental conditions:  $\lambda_{\text{ex}} = 557$  nm, solvent = 2-MTHF, magic angle polarization.

components, respectively, of  $Q(t)$ .<sup>72</sup> In our analysis, we use the solvent longitudinal relaxation time ( $\tau_L$ ) as a measure of  $\tau_S$ .<sup>75</sup>

## Results and Discussion

Photoinduced charge-separation (CS) rate constants for 2a-Zn in 2-MTHF solvent were determined by femtosecond pump-probe transient absorption spectroscopy using methods described previously;<sup>49</sup> in these studies, experimental data were recorded over a temperature range between 80 and 320 K. Spectral evolution following photoexcitation at 557 nm at three

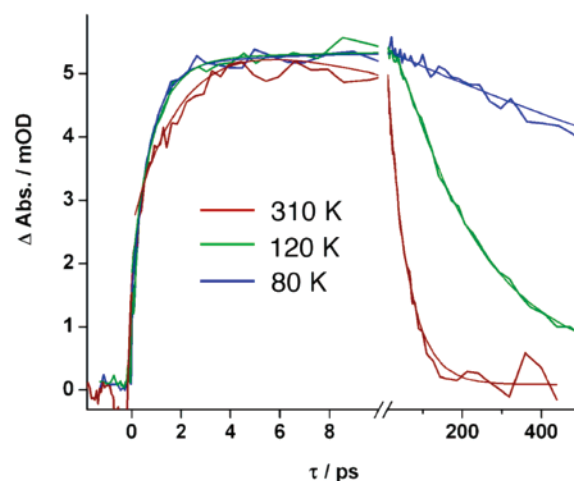
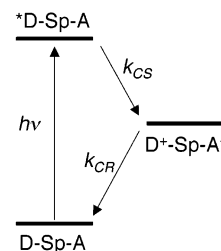


**Figure 2.** Normalized transient decay kinetics determined at 658 nm. The best biexponential function fit for 310 K and the triexponential function fits for 120 and 80 K are depicted by thin lines. Experimental conditions:  $\lambda_{\text{ex}} = 557$  nm, solvent = 2-MTHF, magic angle polarization.

## SCHEME 1: Simplified Photoinduced Charge-Separation and Charge-Recombination Reaction Scheme



representative temperatures (310, 120, and 80 K) is illustrated in Figure 1A–C. Over the entire temperature range, the appearance of a moderately intense transient absorption feature ( $\lambda \sim 680$  nm) corresponding to the absorption of a (porphinato)-zinc(II) cation radical<sup>76</sup> was clearly observed following photoexcitation, signaling the formation of the charge separated state,  $D^+-Sp-A^-$ . Figure 2 highlights the comparative decay kinetics of the transient absorption spectra that are plotted in Figure 1A–C, probed at 658 nm. At temperatures higher than 150 K, these transient decay kinetics were nicely fit by biexponential functions (eq 12) with similar amplitudes for the rise and the decay components. It is thus reasonable to assign the rise component as CS and the decay component as charge recombination (CR), as illustrated in Scheme 1. Below 150 K, however, fitting with a biexponential function yielded results that became increasingly poor with decreasing temperature. In this low-temperature region, only by using a triexponential function with two rise components and one decay component could the data be modeled (eq 13). The slower component ( $k_1$ ,  $\tau_1$ ) exhibited an unusual temperature dependence, whereas the faster component ( $k_2$ ,  $\tau_2$ ) was nearly temperature-independent over all temperature ranges. It is important to note that the ratio of amplitudes of these two components ( $A_1/A_2$ ,  $\tau_1 > \tau_2$ ) became smaller as the temperature decreased (Table 1). The sole decay component ( $\tau_3$ ) is assigned as CR in these cases.

$$CS(t) = A_0 + A_1 \exp(-\tau_1/t) + A_3 \exp(-\tau_3/t) \quad (12)$$

$$CS(t) = A_0 + A_1 \exp(-\tau_1/t) + A_2 \exp(-\tau_2/t) + A_3 \exp(-\tau_3/t) \quad (13)$$

**TABLE 1: Fitting Parameters Describing the Photoinduced Charge-Separation Kinetics for Electronically Excited 2a-Zn<sup>a</sup>**

<i>T</i>	1000/ <i>T</i>	<i>A</i> <sub>1</sub> , %	$\tau_1$ , fs	<i>A</i> <sub>2</sub> , %	$\tau_2$ , fs	<i>A</i> <sub>3</sub> , %	$\tau_3$ , fs	<i>A</i> <sub>1</sub> / <i>A</i> <sub>2</sub>
320 <sup>b</sup>	3.13	−37	2271 ± 192			63	55 572 ± 2362	
310 <sup>b</sup>	3.23	−37	2151 ± 164			63	50 624 ± 1820	
290 <sup>b</sup>	3.45	−37	2326 ± 178			63	41 167 ± 1510	
280 <sup>b</sup>	3.57	−36	2356 ± 188			64	38 922 ± 1418	
270 <sup>b</sup>	3.7	−36	2339 ± 149			64	37 085 ± 1065	
260 <sup>b</sup>	3.85	−34	2934 ± 434			66	37 019 ± 2817	
240 <sup>b</sup>	4.17	−34	3698 ± 495			66	32 865 ± 2363	
220 <sup>b</sup>	4.55	−37	5068 ± 674			63	25 097 ± 1773	
200 <sup>b</sup>	5	−39	5551 ± 401			61	23 979 ± 871	
190 <sup>b</sup>	5.26	−40	7954 ± 779			60	22 416 ± 1312	
180 <sup>b</sup>	5.56	−44	15 581 ± 8462	−5	1232 ± 110	51	19 827 ± 8683	8.8
170 <sup>b</sup>	5.88	−40	9954 ± 1505			60	27 413 ± 2787	
165 <sup>b</sup>	6.06	−41	11 128 ± 1891			59	27 287 ± 2974	
155 <sup>b</sup>	6.45	−42	15 271 ± 2805			58	31 014 ± 3707	
151 <sup>b</sup>	6.62	−43	21 305 ± 5282			57	35 005 ± 5834	
145 <sup>c</sup>	6.9	−33	20 482 ± 4155	−14	882 ± 86	53	44 622 ± 5214	2.4
140 <sup>c</sup>	7.14	−26	18 293 ± 1907	−20	775 ± 51	54	60 330 ± 2874	1.3
135 <sup>c</sup>	7.41	−23	19 542 ± 2129	−24	723 ± 41	53	71 648 ± 2999	1.0
130 <sup>c</sup>	7.69	−19	20 681 ± 2810	−26	744 ± 51	54	103 573 ± 5970	0.7
125 <sup>c</sup>	8	−18	31 695 ± 4793	−28	798 ± 46	54	131 421 ± 5951	0.6
120 <sup>c</sup>	8.33	−12	28 339 ± 3736	−31	877 ± 43	57	207 075 ± 4704	0.4
115 <sup>c</sup>	8.7	−9	16 774 ± 2342	−37	711 ± 37	54	319 168 ± 5408	0.2
110 <sup>c</sup>	9.09	−7	11 728 ± 1778	−46	560 ± 66	47	491 616 ± 9971	0.2
100 <sup>c</sup>	10	−5	6164 ± 3394	−38	705 ± 91	57	1E+06 ± 27 013	0.1
90 <sup>c</sup>	11.11	−7	3668 ± 1643	−39	595 ± 95	54	2E+06 ± 50 632	0.2
80 <sup>c</sup>	12.5	−4	5200 ± 4015	−40	710 ± 92	57	2E+06 ± 54 831	0.1

<sup>a</sup> Kinetic data was acquired using ultrafast transient absorption spectroscopy. Experimental conditions:  $\lambda_{\text{ex}} = 557$  nm,  $\lambda_{\text{probe}} = 658$  nm, solvent = 2-MTHF, magic angle polarization. <sup>b</sup> Determined by the best fit of transient decay kinetics at 658 nm with a biexponential function (eq 1). <sup>c</sup> Determined by the best fit of transient decay kinetics at 658 nm with a triexponential function (eq 2).

**TABLE 2: Fitting Parameters Describing the 2a-Zn Photoinduced Charge-Separation Reaction, Where Vibrationally Unrelaxed and Vibrationally Relaxed S<sub>1</sub> States and S<sub>1</sub>-Manifold Vibrational Relaxation Dynamics are Explicitly Considered (See eq 18)**

<i>T</i> , K	10 <sup>3</sup> / <i>T</i> , K <sup>−1</sup>	<i>A</i> <sub>1</sub> , %	$k_r, \times 10^{12}$	$k_{\text{CS}_2}, \times 10^{12}$	<i>A</i> <sub>2</sub> , %	$k_{\text{CS}_1}, \times 10^{11}$	<i>A</i> <sub>3</sub> , %	$k_{\text{CR}}, \times 10^9$
320 <sup>b</sup>	3.3							
310 <sup>a</sup>	3.2	−23.6	2.90 ± 1.28	3.02 ± 0.93	−26.4	4.17 ± 0.43	50.00	2.00 ± 0.07
290 <sup>a</sup>	3.4	−22.6	2.85 ± 1.20	2.76 ± 0.81	−27.4	3.93 ± 0.41	50.00	2.46 ± 0.09
280 <sup>a</sup>	3.6	−24.9	2.16 ± 0.65	2.52 ± 0.47	−25.1	3.67 ± 0.42	50.00	2.62 ± 0.10
270 <sup>a</sup>	3.7	−25.5	2.00 ± 0.40	2.44 ± 0.30	−24.5	3.53 ± 0.31	50.00	2.77 ± 0.08
260 <sup>a</sup>	3.8	−24.5	1.75 ± 0.43	2.05 ± 0.30	−25.5	3.49 ± 0.44	50.00	2.69 ± 0.19
240 <sup>a</sup>	4.2	−25.7	1.77 ± 0.32	2.16 ± 0.28	−24.3	2.68 ± 0.32	50.00	3.05 ± 0.21
220 <sup>a</sup>	4.5	−23.4	2.07 ± 0.28	2.05 ± 0.23	−26.6	2.08 ± 0.21	50.00	3.92 ± 0.24
200 <sup>a</sup>	5.0	−21.8	0.88 ± 0.07	0.86 ± 0.05	−28.2	1.63 ± 0.16	50.00	4.31 ± 0.20
190 <sup>a</sup>	5.3	−20.7	0.82 ± 0.05	0.71 ± 0.07	−29.3	1.07 ± 0.16	50.00	4.83 ± 0.44
180 <sup>a</sup>	5.6	−20.4	0.75 ± 0.08	0.63 ± 0.11	−29.6	0.82 ± 0.20	50.00	4.70 ± 0.83
170 <sup>b</sup>	5.9							
165	6.1	−16.7	1.13 ± 0.31	0.67 ± 0.36	−33.3	0.58 ± 0.35	50.00	4.73 ± 2.51
155	6.5	−20.7	0.89 ± 0.08	0.73 ± 0.11	−29.3	0.62 ± 0.14	50.00	3.35 ± 0.50
151 <sup>b</sup>	6.6							
145	6.9	−26.3	0.80 ± 0.06	0.98 ± 0.08	−23.7	0.60 ± 0.10	50.00	2.09 ± 0.18
140	7.1	−29.6	0.76 ± 0.04	1.20 ± 0.05	−20.4	0.71 ± 0.07	50.00	1.55 ± 0.06
135	7.4	−32.0	0.63 ± 0.03	1.19 ± 0.05	−18.0	0.57 ± 0.06	50.00	1.37 ± 0.06
130	7.7	−34.2	0.57 ± 0.03	1.32 ± 0.07	−15.8	0.60 ± 0.08	50.00	0.94 ± 0.05
125	8.0	−36.4	0.43 ± 0.03	1.22 ± 0.05	−13.6	0.38 ± 0.05	50.00	0.74 ± 0.03
120	8.3	−39.7	0.35 ± 0.02	1.40 ± 0.04	−10.3	0.51 ± 0.07	50.00	0.47 ± 0.01
115	8.7	−41.5	0.29 ± 0.02	1.48 ± 0.03	−8.5	0.71 ± 0.09	50.00	0.31 ± 0.01
110	9.1	−39.9	0.40 ± 0.05	1.73 ± 0.06	−10.1	1.46 ± 0.23	50.00	0.20 ± 0.01
100	10.0	−42.3	0.29 ± 0.09	1.86 ± 0.09	−7.7	2.70 ± 0.86	50.00	0.09 ± 0.00
90	11.1	−42.1	0.27 ± 0.09	1.76 ± 0.08	−7.9	3.07 ± 0.98	50.00	0.06 ± 0.00
80	12.5	−43.9	0.21 ± 0.08	1.80 ± 0.08	−6.1	2.91 ± 1.17	50.00	0.06 ± 0.00

<sup>a</sup> The two rate constants  $k_r$  and  $k_{\text{CS}_2}$  collapsed into almost the same value. <sup>b</sup> The fitting could not be done accurately.

These experimental results were analyzed within the context of several established ET theories. Comparison of the experimental charge-separation rate constant ( $k_{\text{CS}}$ ;  $k_1$  and  $k_2$ ) temperature dependences to a distribution of theoretically predicted trends is depicted in Figure 3; tabulated experimental and theoretical CS rate-constant values are listed in Table S1. Note that the temperature dependences of the reaction free energy

( $\Delta G$ ) and solvent reorganization energy ( $\lambda_s$ ) were taken into account in these theoretical simulations (Table S2). Analysis of the  $k_1$  component shows three distinct phenomenological temperature dependences in the experimental temperature window; such characteristic variations in the magnitude of  $k_{\text{CS}}$  with temperature have not been observed previously. At relatively high temperatures ( $T \geq 270$  K), the magnitudes of

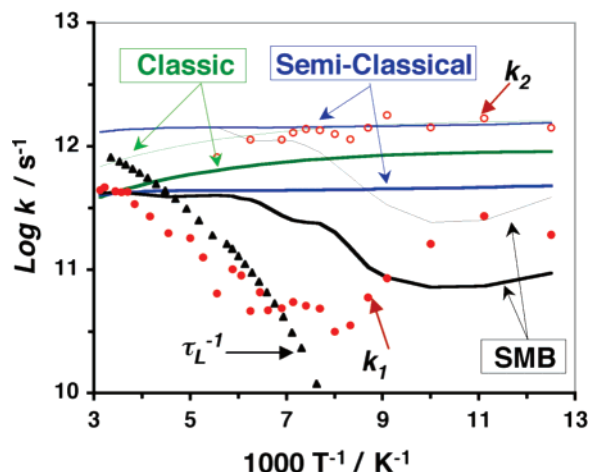


**Figure 3.** Comparison of the experimental temperature dependence of the two observed CS rate constants (open red circles =  $k_1$ ; filled red circles =  $k_2$ ) with those calculated via classical<sup>24</sup> (green thin and thick lines for  $V_{el} = 60$  and  $45 \text{ cm}^{-1}$ , respectively), semiclassical<sup>25,27–29</sup> (blue thin and thick lines for  $V_{el} = 90$  and  $50 \text{ cm}^{-1}$ , respectively), and Sumi–Marcus–Barbara<sup>72,74</sup> (black thin and thick lines for  $V_{el} = 95 \text{ cm}^{-1}$  and  $44 \text{ cm}^{-1}$ , respectively) models. The temperature dependence of the solvent reorganization energy ( $\lambda_s$ ) and reaction free energy ( $\Delta G$ ) were taken into account in these theoretical analyses (Table S2).<sup>11,20</sup> For the semiclassical calculation, an intramolecular reorganization energy  $\lambda_v = 0.5 \text{ eV}$  and an averaged single high-frequency vibrational quantum  $\hbar(\omega) = 1600 \text{ cm}^{-1}$  were used. For the SMB calculation,  $\lambda_v$  was partitioned into  $\lambda_{QM} = 0.35 \text{ eV}$  and  $\lambda_{cl,vib} = 0.15 \text{ eV}$ , where  $\lambda_{QM}$  and  $\lambda_{cl,vib}$  are intramolecular reorganization energies due to the quantum-mechanical high-frequency and classical low-frequency vibrations, respectively. Note that only the  $\tau_{SMB,b}$  component (eq 9)<sup>72</sup> was illustrated in the figure. For  $\tau_{SMB,a}$  values (eq 8), see Table S1. [Because  $k_{SMB,m} = \tau_{SMB,m}^{-1}$ ,  $m = a$  or  $b$ , note that  $\tau_{SMB,a}$  and  $\tau_{SMB,b}$  represent average survival times that emphasize the faster ( $\tau_{SMB,a}$ ) and slower ( $\tau_{SMB,b}$ ) decaying components of the survival probability,  $Q(t)$ .<sup>72</sup> The temperature-dependent inverse longitudinal relaxation times of 2-MTHF ( $\tau_L^{-1}$ ) are shown as black triangles.<sup>75</sup>

the  $k_1$  rate constants are weakly dependent on the temperature and decrease only slightly as temperature decreases. This trend in the  $k_1$  magnitudes becomes significantly more pronounced with decreasing temperature over the  $150 \text{ K} \leq T \leq 260 \text{ K}$  range. The  $k_1$  magnitudes then increase sharply in the low-temperature region ( $T < 150 \text{ K}$ ); note, for example, that the  $k_1$  rate constant at  $90 \text{ K}$  is an order of magnitude larger than that determined at  $125 \text{ K}$ . As illustrated in Figure 3, classical, semiclassical, and SMB theories do not model the experimental data accurately and suggest that a possible interpretation of these trends in the temperature-dependent photoinduced **2a-Zn** charge-separation rate constants may involve one or more transitions between various ET mechanisms.

An apparent Arrhenius-type temperature dependence is evident in the medium-to-high-temperature region ( $T > 150 \text{ K}$ ), where the CS reaction is well-described by a monoexponential decay profile. A  $\ln(k\sqrt{T})$  versus  $T^{-1}$  plot of the data in this temperature region suggests two different linear regimes (Figure 4); the activation barriers for these two regions were evaluated to be  $0.51$  and  $1.62 \text{ kcal/mol}$  for the high ( $260 \text{ K} < T < 320 \text{ K}$ ) and medium ( $150 \text{ K} < T < 260 \text{ K}$ ) temperature domains, respectively. Electronic coupling matrix elements ( $V_{el}$ ) were determined in this analysis to be  $190$  and  $503 \text{ cm}^{-1}$  for the high- and medium-temperature regions, though it should be emphasized that these values may not be physically meaningful because the analysis employing eq 2 is based on the assumption that the total reorganization energy and the reaction free energy are constant within the relevant temperature region. Note that

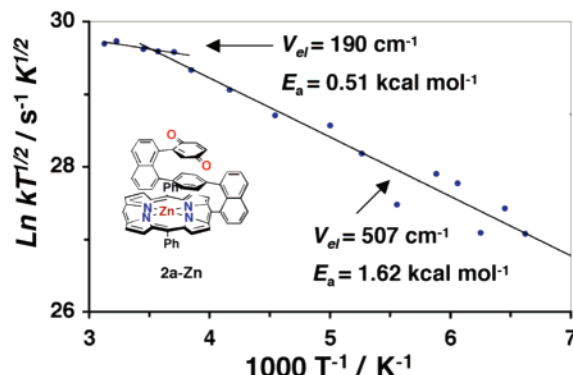


**Figure 4.** Arrhenius analysis of the  $k_1$  CS rate constant. Deduced electronic coupling matrix elements and activation barriers for the two apparent linear regimes are shown as insets.

solvent reorganization energies calculated with the Marcus expression (eq 5) with temperature-dependent dielectric constants are relatively invariable over the  $150\text{--}320 \text{ K}$  temperature domain ( $0.48 < \lambda_T < 0.50$ ); in contrast, the reaction free energies determined using a Weller model (eq 4) are temperature-dependent, ranging from  $-0.81 \text{ eV}$  at  $320 \text{ K}$  to  $-0.97 \text{ eV}$  at  $150 \text{ K}$  (Table S2). Furthermore, these simple analyses suggest a greater than twofold increase in the evaluated magnitudes of  $V_{el}$  with an  $\sim 100 \text{ K}$  decrease in temperature. Considering the fact that classical, semi-classical, and SMB theories (eqs 1, 6, and 9) predict very similar electronic coupling values for the CS reactions ( $44\text{--}50 \text{ cm}^{-1}$ ), the extracted  $503 \text{ cm}^{-1}$  value for  $V_{el}$  in the medium-temperature region suggests that at least in this temperature domain the apparent temperature dependence cannot be attributed purely to a thermal activation barrier.

Interestingly, the temperature-dependent component of the experimental ET dynamics ( $k_1$ ) in the medium-temperature region was found to mimic the sharply decreasing pattern of the solvent longitudinal relaxation rate constants ( $\tau_L^{-1}$ ) (Figure 3), suggesting that in this temperature region the CS reaction is strongly coupled to the solvent dynamics. To further probe this possibility, we simulated experimental ET rate constants using the theoretical framework developed by Rips and Jortner.<sup>34</sup> The ET rate constant in the solvent-controlled adiabatic regime can be expressed as

$$k_{SC} = \frac{k_{NA}}{(1 + \kappa_A)^\beta} \quad (14)$$

$$\kappa_A = \frac{4\pi V_{el}^2 \tau_L}{\hbar \lambda_s} \quad (15)$$

where  $k_{NA}$  is the nonadiabatic ET rate from the eq 1,  $\kappa_A$  is the adiabaticity parameter, and  $\beta$  is the solvent dielectric relaxation parameter from the Davidson–Cole dielectric relaxation spectrum (eq 16).<sup>77,78</sup>

$$\hat{\epsilon}(\omega) = \epsilon_\infty + \frac{(\epsilon_0 - \epsilon_\infty)}{(1 + i\omega\tau_0)^\beta} \quad (16)$$

The simulated  $k_{SC}$  values are plotted along with experimental  $k_1$  data (green diamonds) in Figure 5. This system features a moderate-to-large solvent adiabaticity parameter ( $2.0_{T=260} < \kappa_A < 19.6_{T=150}$ , eq 15); when a constant value of  $\beta = 1$  for the solvent dielectric relaxation parameter is used (solid red triangles), the predicted  $k_{SC}$  values overestimate the solvent-controlled adia-

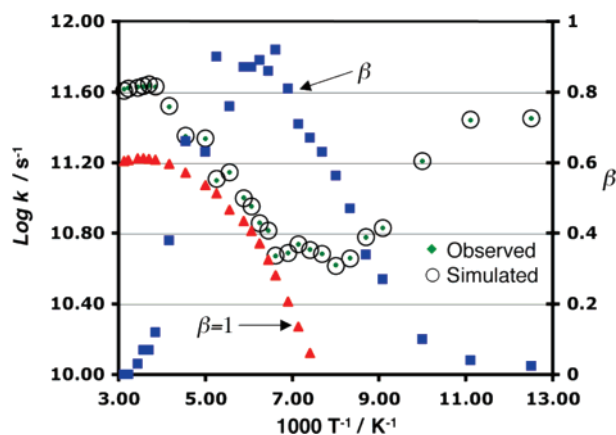


**Figure 5.** Comparison of experimental temperature dependence of the CS-state formation rate constant (green diamonds) with those calculated with the Rips/Jortner Model (eq 14). For the calculation of  $k_{\text{NA}}$ , eq 1 was used, and  $V_{\text{el}}$  was fixed at 46  $\text{cm}^{-1}$ . Red triangles represent simulated charge-separation rate constants computed with a solvent dielectric relaxation parameter  $\beta = 1$ . The black open circles represent CS rate constants simulated to match the experimental values, with variable  $\beta$  values, which are plotted as blue squares.

batic effect. Values of  $k_{\text{SC}}$  with  $\beta$  values smaller than 1 cannot reproduce the experimental result accurately. Treating  $\beta$  as a variable parameter, the set of computed rate constants that best described experimental results were obtained (green diamonds, Figure 5); the  $\beta$  values used in these computations are co-plotted in Figure 5 as blue squares. Even though the incorporation of  $\beta$  in eq 14 stems from the Davidson–Cole dielectric relaxation spectrum (eq 16),<sup>77,78</sup> which in contrast to the Debye model characterizes the heterogeneous distribution of the solvent dielectric relaxation time, the smooth change of  $\beta$  values in Figure 5 cannot be linearly related to the change of solvent dielectric relaxation parameter. We suggest that this temperature dependence of  $\beta$  values is consistent with a gradual transition of the ET mechanism from nonadiabatic at high temperature, to solvent-controlled adiabatic in the mid-temperature region, to one where solvent dynamics become decoupled from photoinduced ET at temperatures below 150 K.<sup>77,78</sup>

It is appropriate to mention that solvent-controlled adiabatic ET reactions are expected to occur more commonly in the normal region because in the activationless and inverted regimes ET events can be promoted by quantum-mechanical nuclear tunneling, which are little influenced by solvent dynamics.<sup>1,3</sup> In **2a-Zn**, the magnitude of the computed reaction free energy ( $\Delta G = -0.81$  eV) at 320 K is indeed  $\sim 0.17$  eV smaller than the total reorganization energy ( $\lambda_{\text{S}} = 0.48$ ,  $\lambda_{\text{V}} = 0.5$  eV), suggesting that the CS reaction resides within the Marcus normal region.  $\Delta G_{\text{CS}}$  changes smoothly with decreasing temperature, and drives the reaction from the activationless region ( $T \sim 120$ – $125$  K) to the inverted region at temperatures below 120 K. For this reason, the magnitude of  $k_1$  is minimally affected by the solvent degrees of freedom at temperatures below 120 K, and a departure from the solvent-controlled adiabatic regime for the CS reaction is manifest.<sup>79</sup>

We considered that the sharp increase in the magnitude of the experimental  $k_1$  ET rate constant measured for **2a-Zn** as a function of decreasing temperature in the low-temperature ( $T < 150$  K) region may derive from augmented Franck–Condon (FC) overlap. Because the reaction energetics evolve smoothly from the Marcus normal to the Marcus inverted regions as temperature decreases, it is anticipated that nuclear wavefunction overlap will increase with decreasing temperature and thus magnify the magnitude of the CS rate constant. Computation

of the temperature-dependent FC factors (eq 17) suggests that this parameter changes only modestly over substantial temperature regimes; for example, this analysis gives the values of the FC factor at 150 and 80 K of 1.19 and 1.12, respectively.

$$(FC) = \frac{1}{\sqrt{4\pi\lambda_{\text{cl}} k_{\text{B}} T}} \exp(-S_{\text{c}}) \sum_{m=0}^{\infty} \frac{S_{\text{c}}^m}{m!} \exp\left(-\frac{(\Delta G + \lambda_{\text{cl}} + m\hbar\langle\omega\rangle)^2}{4\lambda_{\text{cl}} k_{\text{B}} T}\right) \quad (17)$$

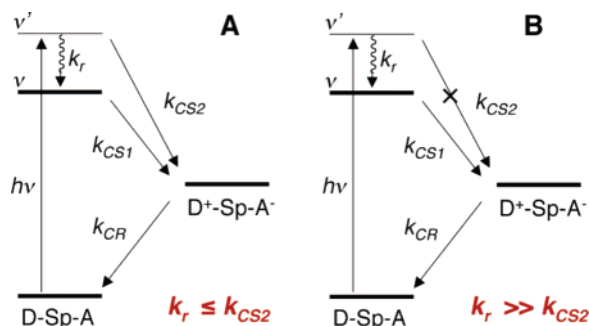
Although the nature of the ET dynamics becomes more complex as it gradually decouples from solvent dynamics, the exact genesis for the sharp observed increase in the magnitude of the temperature-dependent CS rate constant ( $k_1$ ) with decreasing temperature in the low-temperature region remains obscure.

The temperature independence of the  $k_2$  component of the CS dynamics arises likely from the involvement of a dominant quantum-mechanical intramolecular vibrational degree of freedom for this reaction. Rate constants simulated using the semiclassical rate expression (eq 6) are denoted by the thin blue line in Figure 3; note that this theoretical simulation mirrors the experimentally determined values for  $k_2$  well within the low-temperature region ( $T < 150$  K). Notably, kinetic data simulated using the classical Marcus expression (eq 1) (thin green line) also model the  $k_2$  experimental data well (Figure 3); in contrast, the SMB model, which considers the vibrational degrees of freedom of the reactant state as well as those of product state, describe experimental results rather poorly (thin black line). Although these analyses might support a hypothesis that high-frequency intramolecular vibrational degrees of freedom do not play an important role in determining the temperature-dependent magnitude of  $k_2$  values, it should be noted that the **2a-Zn** charge-separation energetics suggest that reaction occurs at or near the Marcus maximum rate constant. As a result, a severe temperature dependence cannot be manifest because of the very small activation barrier, and thus it is not surprising that all three theoretical models predict weak temperature dependence of the CS  $k_2$  value.

As noted earlier, below 150 K the amplitude of the  $k_2$  CS component increased relative to the temperature-dependent  $k_1$  CS component (Figure 3). Deduced  $V_{\text{el}}$  values for the temperature-independent  $k_2$  CS reaction using classical, semiclassical, and SMB models were 60, 64, and 90  $\text{cm}^{-1}$ , respectively. The respective electronic coupling matrix elements computed with the same models for the  $k_1$  component were 46, 36, and 50  $\text{cm}^{-1}$ . With respect to the larger magnitude  $V_{\text{el}}$  value determined for  $k_2$ , note that the time scale of the  $k_2$  component is comparable to that for intramolecular vibrational energy redistribution (IVR) in the (porphinato)zinc(II)  $S_1$  state manifold.<sup>80–85</sup> Because the **12a-Zn\*** state was prepared using laser excitation having excess energy ( $\sim 0.17$  eV) relative to the  $S_0(\nu = 0) \rightarrow S_1(\nu = 0)$  transition, a competition between vibronic relaxation to an equilibrated  $S_1$  state and direct ET to the CS state from the vibrationally unrelaxed **12a-Zn\*** state without influence of the solvent coordinate is possible. Although there have been a number of reports that emphasized the competition between vibrational relaxation and electron transfer within the CS state manifold,<sup>86</sup> relatively few studies have probed such competitive dynamics for ultrafast charge-separation or injection.<sup>87–92</sup> Scheme 2A describes a scenario where ET from the vibrationally unrelaxed **2a-Zn** singlet excited state occurs faster or comparable to the  $S_1$  vibrational manifold relaxation rate. On the basis



**SCHEME 2: Reaction Schemes Describing (A) Vibrational Relaxation and Electron Transfer from a Vibrationally Excited  $S_1$  State, and (B) an Identical CS Reaction but with No Contribution from  $CS_2$**



of the reaction scheme in Scheme 2A, the kinetics of transient decay of CS state are given by eq 18:

$$CS(t) = A_0[A_1 \exp(-k_e t) + A_2 \exp(-k_{CS1} t) + A_3 \exp(-k_{CR} t)] + C \quad (18)$$

Here,  $k_e = k_r + k_{CS2}$ ,  $A_1 = [k_{CS2}/(k_{CR} - k_e) + k_r k_{CS1}/(k_{CR} - k_e)(k_{CS1} - k_e)]$ ,  $A_2 = [k_r k_{CS1}/(k_{CS1} - k_e)(k_{CS1} - k_{CR})]$ ,  $A_3 = [k_r k_{CS1}/(k_{CS1} - k_e)(k_{CR} - k_{CS1}) - k_{CS2}/(k_{CR} - k_e) - k_r k_{CS1}/(k_{CR} - k_e)(k_{CS1} - k_e)]$ . The experimental temperature-dependent transient absorption dynamics probed at 658 nm were reanalyzed with eq 18; this model is depicted in Figure 6, which highlights the temperature-dependent values determined for  $S_1$  manifold vibrational relaxation ( $k_r$ ), CS from the vibronically equilibrated singlet excited state ( $k_{CS1}$ ), and CS from the vibrationally unrelaxed **2a-Zn**  $S_1$  state ( $k_{CS2}$ ). This analysis predicts that the vibronic relaxation component ( $k_r$ ) is ultrafast ( $k_r > 1 \text{ ps}^{-1}$ ) at 310 K and decreases gradually with decreasing temperature, until  $\sim 120 \text{ K}$ , where it remains near constant at  $\sim 0.2 \text{ ps}^{-1}$ . The evaluated  $k_{CS2}$  rate constant at temperatures between 310 and 180 K mirrored the magnitudes determined for  $k_r$  in this model. At temperatures below 180 K,  $k_{CS2}$  exceeds  $k_r$  and increases gradually until it reaches its maximal values of  $\sim 1.8 \text{ ps}^{-1}$  at 100 K. It is important to note that this refined analysis (eq 18) will not model scenarios well where either  $k_r$  or  $k_{CS2}$  approach zero (e.g., Scheme 2B); hence,  $k_{CS2}$  values determined at temperatures higher than 180 K and  $k_r$  values determined at temperatures lower than 100 K will express large associated errors. Figure 6 shows clearly the distinctive temperature dependences of these three components. The temperature dependence of the  $S_1$  manifold vibrational relaxation rate constant of the initially prepared **12a-Zn**\* state is noteworthy, given the fact that it plays a highly unusual but key role in determining the temperature-dependent ET dynamics, and that the  $k_r$  magnitude determined at 310 K mirrors that evaluated independently for electronically excited (porphinato)zinc(II) complexes.<sup>80–85</sup>

With this refined model, the electronic coupling matrix element ( $V_{el}$ ) for the  $CS_2$  process was recalculated.<sup>93</sup> Semiclassical and SMB models gave values of 100 and 150  $\text{cm}^{-1}$ , respectively, for the  $CS_2$  electronic coupling matrix element. It is interesting that these  $V_{el}$  values are more than a factor of 2 larger than those evaluated using an analysis that did not consider a vibrationally unrelaxed **2a-Zn**  $S_1$  excited state. The classical model could not reproduce the temperature-independent experimental CS component that became more prominent with increased reaction free energy, mainly because of the revival of the activation barrier manifest in the Marcus inverted region.

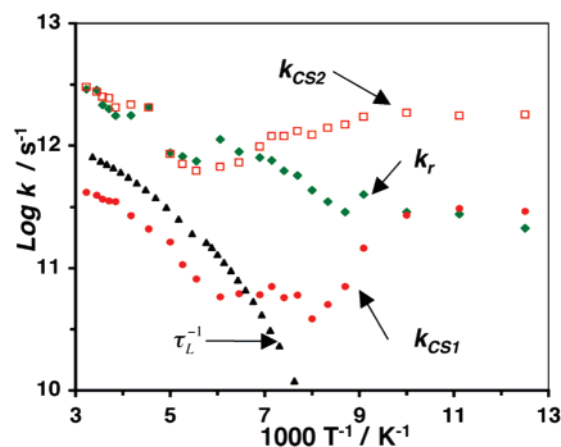


**Figure 6.** Temperature dependence of the photoinduced charge-separation rate constants for vibrationally unrelaxed (red open squares,  $k_{CS2}$ ) and relaxed (red circles,  $k_{CS1}$ ) **2a-Zn**  $S_1$  states. The temperature-dependent  $S_1$  manifold vibrational relaxation rate constants are shown as green diamonds; see eq 18. The temperature-dependent solvent longitudinal relaxation rate constants ( $\tau_L^{-1}$ ) for 2-MTHF are depicted as black triangles.

It is noteworthy that both semiclassical and SMB models predict  $V_{el}$  values more than a factor of 2 larger for charge separation from a vibrationally unrelaxed **12a-Zn**\* state relative to that manifest for the analogous equilibrated  $S_1$  state species. The extent to which vibrationally relaxed and vibrationally unrelaxed excited states feature disparate donor–acceptor electronic coupling has not been interrogated previously, due to the fact that systems that manifest two such measurable rate processes simultaneously have heretofore lacked precedent.

In contrast to the  $k_2$  CS component of eq 13, which features dynamic contributions from  $k_{CS2}$  and  $k_r$ ,  $k_{CS1}$  determined from the eq 18 analysis is virtually invariant with respect to the  $k_1$  component determined from the model described by eq 13. The amplitude of the  $k_1$  ( $k_{CS1}$ ) component determined by eq 13 decreased continuously from 33% at 145 K to 4% at 80 K, whereas that of  $k_2$  ( $k_{CS2} + k_r$ ) increased from 14% at 145 K to 40% at 80 K. The amplitude of the  $k_{CS1}$  component evaluated using eq 18 was 39.5% at 165 K and decreased steadily to 6.1% at 80 K. The amplitude of combined  $k_{CS2}$  and  $k_r$  components increased accordingly with decreasing temperature, highlighting the fact that ET from the vibrationally unrelaxed **12a-Zn**\* state becomes dominant with decreasing temperature.

These complex temperature-dependent **12a-Zn**\* CS mechanisms can be summarized using a Sumi–Marcus two-dimensional free-energy surface model (Figure 7):

(1) At high temperatures (e.g., 320 K), the  $S_1$  manifold vibrational relaxation rate constant ( $k_r$ ) is ultrafast ( $\log k_r > 12 \text{ s}^{-1}$ ) and exceeds both established CS rate constants ( $k_{CS1}$  and  $k_{CS2}$ , Figure 6). In this temperature limit, the vibrationally excited  $S_1$  state relaxes quickly to an quasi-equilibrated (relaxed)  $S_1$  state. The time scale of the solvent dynamics ( $\tau_L$ ) is also very fast ( $\sim 1 \text{ ps}$ ). Because the observed CS time constant ( $\sim 2 \text{ ps}$ ) exceeds that for solvent dynamics, a nonadiabatic mechanism is manifest (Figure 7A).

(2) At moderately low temperatures (e.g., 160 K),  $k_r$  is still larger than  $k_{CS2}$  (Figure 6). The relative yield of the charge-separated product from the vibrationally unrelaxed  $S_1$  state is small relative to that produced from vibrationally relaxed **12a-Zn**\* because the time constant determined for  $S_1$  manifold vibrational relaxation is  $\sim 1.3 \text{ ps}$ . CS, however, is also strongly coupled to solvent degrees of freedom in this temperature regime. The longitudinal relaxation time of the solvent is  $\sim 11$

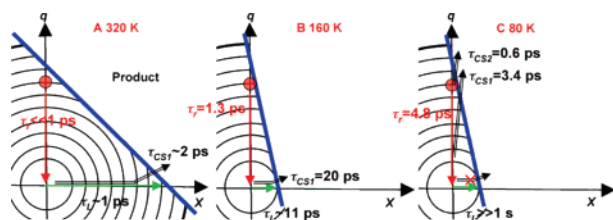


**Figure 7.** Diagrams based on Sumi–Marcus two-dimensional free energy surfaces that illustrate the  $^{12}\text{a-Zn}^*$  reaction dynamics at three different temperatures. Contours of evenly spaced energies are drawn only for the reactant states. The thick blue line represents the intersection between two surfaces; the abscissa ( $X$ ) and the ordinate ( $q$ ) represent solvent and vibrational coordinates, respectively. The red circle on the  $q$  axis corresponds to the initially prepared, vibrationally excited  $S_1$  state. The red and green arrows represent vibrational relaxation and solvent fluctuation, respectively. The ET process is represented as a black arrow.

ps and CS occurs on  $\sim 20$  ps time scale. It is important to note that the activation barrier at this temperature is much lower than that at 320 K; however, the barrier is still nonzero, and the ET time constant is governed by the solvent fluctuation time scale. As temperature decreases further, the activation barrier vanishes and ET can occur only by vibrational excitation without the aid of solvent fluctuation. The coupling of CS dynamics to solvent degrees of freedom thus becomes weaker. Simultaneously, because  $k_r$  diminishes relative to  $k_{CS_2}$ , the direct transition of a fraction of the vibrationally unrelaxed excited-state population to the CS state becomes possible (Figure 7B).

(3) At the lowest probed temperatures (e.g., 80 K), efficient conversion of vibrationally unrelaxed  $^{12}\text{a-Zn}^*$  to the CS state is manifest, as  $k_{CS_2} > k_r$ .

## Conclusions

The mechanism of photoinduced electron-transfer dynamics in a rigid, cofacially aligned (porphinato)zinc(II)-spacer-quinone molecule (**2a-Zn**) has been interrogated using ultrafast transient absorption spectroscopy to measure the temperature dependence of charge-separation (CS) rate constants in 2-MTHF solvent between 80 and 320 K. The initial analyses of transient decay kinetics probed at 658 nm after photoexcitation with 557 nm light, using bi- and triexponential functions, showed that changes in the CS state population occur via one rise and one decay component at temperatures exceeding 150 K, and via one decay and two rise components at temperatures lower than 150 K. The rise components were assigned to charge-separation processes, and the decay component to charge recombination. These analyses were refined with a kinetic model that considered that CS proceeds from both vibrationally relaxed and unrelaxed **2a-Zn**  $S_1$  states (Scheme 2). At relatively high temperatures, vibronic relaxation is ultrafast and the charge-separation reaction occurs primarily from a vibrationally relaxed  $S_1$  state. Solvent dynamics represented by the longitudinal relaxation time ( $\tau_L^{-1}$ ) are slightly faster than that of the CS reaction; CS thus occurs nonadiabatically along the solvent coordinate with  $V_{el} \sim 50$   $\text{cm}^{-1}$ . As the temperature decreases, the CS time scale from the relaxed **2a-Zn**  $S_1$  state approaches that of solvent dynamics. With these time scales and a moderately large electronic coupling, the CS reaction falls into the solvent-controlled adiabatic regime. As temperature decreases further, the reaction no longer lies in the solvent-controlled adiabatic regime because the reaction energetics approach the Marcus activationless region. At the lowest probed temperatures, the vibrational relaxation rate constant within the  $S_1$  manifold becomes slower than that for CS from the vibrationally unrelaxed  $^{12}\text{a-Zn}^*$  state;

charge-separation thus derives primarily from a vibronically excited  $S_1$ -state at extremely low temperatures. Through the interplay of these factors, the CS mechanism exhibits a continuous transition from the solvent-controlled adiabatic regime to one governed by nuclear tunneling within an upper vibronic state of the  $S_1$  manifold.

In summary, this study demonstrates: (1) A dominant photoinduced charge-separation pathway at low temperature ( $T < 150$  K) that originates from a vibrationally unrelaxed  $S_1$  state. These dynamics derive from the facts that (i) the initially prepared  $S_1$  state by the laser excitation features  $\sim 0.17$  eV of excess energy and a  $V_{el}$  value significantly larger than that for the relaxed  $S_1$  state and (ii) the  $S_1$  manifold vibrational relaxation rate constant ( $k_r$ ) decreases with decreasing temperature. (2) An unusual solvent-controlled adiabatic ET in moderately polar 2-MTHF solvent ( $\epsilon_S \sim 14$  at 150 K, the temperature at which the degree of solvent-controlled adiabaticity is maximized). (3) A transition from the solvent-controlled adiabatic regime to one where charge separation is governed by nuclear tunneling within an upper vibronic state of the  $S_1$  manifold. Over this mechanistic transition, the CS rate constants increased by approximately 1 order of magnitude, driven in part by the reaction energetics, which showed a smooth change from normal-to-inverted region with decreasing temperature. (4) A rare example of a system where temperature-dependent photoinduced charge-separation (CS) dynamics from vibrationally relaxed and unrelaxed  $S_1$  states can be differentiated. (5) A temperature-dependent mechanistic transition of photoinduced CS from the nonadiabatic to the solvent-controlled adiabatic regime, followed by a second temperature-dependent mechanistic evolution where CS becomes decoupled from solvent dynamics and is determined by the extent to which the vibrationally unrelaxed  $S_1$  state is populated.

**Acknowledgment.** This work was supported by a grant from the Division of Chemical Sciences, Office of Basic Energy Research, U.S. Department of Energy (DE-FGO2-02ER15299). We acknowledge the University of Pennsylvania Nano/Bio Interface Center, supported through the National Science Foundation (NSEC DMR-0425780), for infrastructural support. Y.K.K. thanks Dr. Roland Böhrer and Dr. Ranco Richert for kindly providing temperature-dependent dielectric relaxation data for 2-MTHF. Y.K.K. also thanks Dr. Yung Sam Kim for the mathematical support and helpful discussions.

**Supporting Information Available:** Tabulated temperature-dependent ET rate data and analyses. This material is available free of charge via the Internet at <http://pubs.acs.org>.

## References and Notes

- Marcus, R. A.; Sutin, N. *Biochim. Biophys. Acta* **1985**, *811*, 265.
- DeVault, D. *Quantum-Mechanical Tunneling in Biological Systems*, 2nd ed.; Cambridge University Press: Cambridge, 1984.
- Bixon, M.; Jortner, J. *Adv. Chem. Phys.* **1999**, *106*, 35.
- Bagchi, B.; Gayathri, N. *Adv. Chem. Phys.* **1999**, *107*, 1.
- Hopfield, J. J. *Proc. Natl. Acad. Sci. U.S.A.* **1974**, *71*, 3640.
- Harrison, R. J.; Pearce, B.; Beddard, G. S.; Cowan, J. A.; Sanders, J. K. M. *Chem. Phys.* **1987**, *116*, 429.
- Heitele, H.; Michel-Beyerle, M. E.; Finckh, P. *Chem. Phys. Lett.* **1987**, *138*, 237.
- Smit, K. J.; Warman, J. M.; De Haas, M. P.; Paddon-Row, M. N.; Oliver, A. M. *Chem. Phys. Lett.* **1988**, *152*, 177.
- Finckh, P.; Heitele, H.; Volk, M.; Michel-Beyerle, M. E. *J. Phys. Chem.* **1988**, *92*, 6584.
- Gunner, M. R.; Dutton, P. L. *J. Am. Chem. Soc.* **1989**, *111*, 3400.
- Liang, N.; Miller, J. R.; Closs, G. L. *J. Am. Chem. Soc.* **1989**, *111*, 8740.
- Liang, N.; Miller, J. R.; Closs, G. L. *J. Am. Chem. Soc.* **1990**, *112*, 5353.

- (13) Delaney, J. K.; Mauzerall, D. C.; Lindsey, J. S. *J. Am. Chem. Soc.* **1990**, *112*, 957.
- (14) O'Driscoll, E.; Simon, J. D. *J. Am. Chem. Soc.* **1990**, *112*, 6580.
- (15) Rodriguez, J.; Kirmaier, C.; Johnson, M. R.; Friesner, R. A.; Holten, D.; Sessler, J. L. *J. Am. Chem. Soc.* **1991**, *113*, 1652.
- (16) Liu, J. Y.; Bolton, J. R. *J. Phys. Chem.* **1992**, *96*, 1718.
- (17) Zeng, Y.; Zimmt, M. B. *J. Phys. Chem.* **1992**, *96*, 8395.
- (18) Chen, P.; Mecklenburg, S. L.; Meyer, T. J. *J. Phys. Chem.* **1993**, *97*, 13126.
- (19) Kroon, J.; Oevering, H.; Verhoeven, J. W.; Warman, J. M.; Oliver, A. M.; Paddon-Row, M. N. *J. Phys. Chem.* **1993**, *97*, 5065.
- (20) Khundkar, L. R.; Perry, J. W.; Hanson, J. E.; Dervan, P. B. *J. Am. Chem. Soc.* **1994**, *116*, 9700.
- (21) Wiederrecht, G. P.; Svec, W. A.; Wasielewski, M. R. *J. Phys. Chem. B* **1999**, *103*, 1386.
- (22) Davis, W. B.; Ratner, M. A.; Wasielewski, M. R. *J. Am. Chem. Soc.* **2001**, *123*, 7877.
- (23) Napper, A. M.; Read, I.; Waldeck, D. H.; Kaplan, R. W.; Zimmt, M. B. *J. Phys. Chem. A* **2002**, *106*, 4784.
- (24) Marcus, R. A. *J. Chem. Phys.* **1956**, *24*, 966.
- (25) Levich, V. G. *Adv. Electrochem. Eng.* **1966**, *4*, 249.
- (26) Marcus, R. A.; Eyring, H. *Annu. Rev. Phys. Chem.* **1964**, *15*, 155.
- (27) Efrima, S.; Bixon, M. *Chem. Phys. Lett.* **1974**, *25*, 34.
- (28) Van Duyne, R. P.; Fisher, R. S. *Chem. Phys.* **1974**, *5*, 183.
- (29) Jortner, J. *J. Chem. Phys.* **1976**, *64*, 4860.
- (30) Siders, P.; Marcus, R. A. *J. Am. Chem. Soc.* **1981**, *103*, 748.
- (31) Heitele, H.; Pöllinger, F.; Weeren, S.; Michel-Beyerle, M. E. *Chem. Phys. Lett.* **1990**, *168*, 598.
- (32) Zusman, L. D. *Chem. Phys.* **1980**, *49*, 295.
- (33) Hynes, J. T. *J. Phys. Chem.* **1986**, *90*, 3701.
- (34) Rips, I.; Jortner, J. *Chem. Phys. Lett.* **1987**, *133*, 411.
- (35) Åkesson, E.; Walker, G. C.; Barbara, P. F. *J. Chem. Phys.* **1991**, *95*, 4188.
- (36) Walker, G. C.; Barbara, P. F.; Doorn, S. K.; Dong, Y.; Hupp, J. T. *J. Phys. Chem.* **1991**, *95*, 5712.
- (37) Kliner, D. A. V.; Tominaga, K.; Walker, G. C.; Barbara, P. F. *J. Am. Chem. Soc.* **1992**, *114*, 8323.
- (38) Tominaga, K.; Kliner, D. A. V.; Johnson, A. E.; Levinger, N. E.; Barbara, P. F. *J. Chem. Phys.* **1993**, *98*, 1228.
- (39) Kobayashi, T.; Takagi, Y.; Kandori, H.; Kemnitz, K.; Yoshihara, K. *Chem. Phys. Lett.* **1991**, *180*, 416.
- (40) Nagasawa, Y.; Yartsev, A. P.; Tominaga, K.; Johnson, A. E.; Yoshihara, K. *J. Chem. Phys.* **1994**, *101*, 5717.
- (41) Yoshihara, K.; Tominaga, K.; Nagasawa, Y. *Bull. Chem. Soc. Jpn.* **1995**, *68*, 696.
- (42) Pöllinger, F.; Heitele, H.; Michel-Beyerle, M. E.; Anders, C.; Futscher, M.; Staab, H. A. *Chem. Phys. Lett.* **1992**, *198*, 645.
- (43) Heitele, H.; Pöllinger, F.; Haeberle, T.; Michel-Beyerle, M. E.; Staab, H. A. *J. Phys. Chem.* **1994**, *98*, 7402.
- (44) Kosower, E. M.; Dodiuk, H.; Tanizawa, K.; Ottolenghi, M.; Orbach, N. *J. Am. Chem. Soc.* **1975**, *97*, 2167.
- (45) Huppert, D.; Kanety, H.; Kosower, E. M. *Faraday Discuss.* **1982**, *161*.
- (46) Iovine, P. M.; Kellett, M. A.; Redmore, N. P.; Therien, M. J. *J. Am. Chem. Soc.* **2000**, *122*, 8717.
- (47) Kang, Y. K.; Rubtsov, I. V.; Iovine, P. M.; Chen, J. X.; Therien, M. J. *J. Am. Chem. Soc.* **2002**, *124*, 8275.
- (48) Zheng, J. R.; Kang, Y. K.; Therien, M. J.; Beratan, D. N. *J. Am. Chem. Soc.* **2005**, *127*, 11303.
- (49) Rubtsov, I. V.; Susumu, K.; Rubtsov, G. I.; Therien, M. J. *J. Am. Chem. Soc.* **2003**, *125*, 2687.
- (50) Weller, A. *Z. Phys. Chem. N. F.* **1982**, *133*, 93.
- (51) Marcus, R. A. *J. Chem. Phys.* **1965**, *43*, 679.
- (52) Maroncelli, M.; Macinnis, J.; Fleming, G. R. *Science* **1989**, *243*, 1674.
- (53) Kosower, E. M.; Huppert, D. *Chem. Phys. Lett.* **1983**, *96*, 433.
- (54) McGuire, M.; McLendon, G. *J. Phys. Chem.* **1986**, *90*, 2549.
- (55) Simon, J. D.; Su, S. G. *J. Phys. Chem.* **1988**, *92*, 2395.
- (56) Kang, T. J.; Kahlow, M. A.; Giser, D.; Swallen, S.; Nagarajan, V.; Jarzeba, W.; Barbara, P. F. *J. Phys. Chem.* **1988**, *92*, 6800.
- (57) Calef, D. F.; Wolynes, P. G. *J. Phys. Chem.* **1983**, *87*, 3387.
- (58) Calef, D. F.; Wolynes, P. G. *J. Chem. Phys.* **1983**, *78*, 470.
- (59) Garg, A.; Onuchic, J. N.; Ambegaokar, V. *J. Chem. Phys.* **1985**, *83*, 4491.
- (60) Onuchic, J. N. *J. Chem. Phys.* **1987**, *86*, 3925.
- (61) Rips, I.; Jortner, J. *J. Chem. Phys.* **1987**, *87*, 2090.
- (62) Rips, I.; Jortner, J. *J. Chem. Phys.* **1987**, *87*, 6513.
- (63) Jortner, J.; Bixon, M. *J. Chem. Phys.* **1988**, *88*, 167.
- (64) Spargaglione, M.; Mukamel, S. *J. Phys. Chem.* **1987**, *91*, 3938.
- (65) Spargaglione, M.; Mukamel, S. *J. Chem. Phys.* **1988**, *88*, 1465.
- (66) Spargaglione, M.; Mukamel, S. *J. Chem. Phys.* **1988**, *88*, 3263.
- (67) McManis, G. E.; Gochev, A.; Weaver, M. J. *Chem. Phys.* **1991**, *152*, 107.
- (68) Morillo, M.; Cukier, R. I. *J. Chem. Phys.* **1988**, *89*, 6736.
- (69) Masad, A.; Huppert, D.; Kosower, E. M. *Chem. Phys.* **1990**, *144*, 391.
- (70) Sinks, L. E.; Wasielewski, M. R. *J. Phys. Chem. A* **2003**, *107*, 611.
- (71) Liu, M.; Ito, N.; Maroncelli, M.; Waldeck, D. H.; Oliver, A. M.; Paddon-Row, M. N. *J. Am. Chem. Soc.* **2005**, *127*, 17867.
- (72) Sumi, H.; Marcus, R. A. *J. Chem. Phys.* **1986**, *84*, 4894.
- (73) Barbara, P. F.; Walker, G. C.; Smith, T. P. *Science* **1992**, *256*, 975.
- (74) Walker, G. C.; Åkesson, E.; Johnson, A. E.; Levinger, N. E.; Barbara, P. F. *J. Phys. Chem.* **1992**, *96*, 3728.
- (75) Because a CT absorption band is not observed for **2a-Zn**, the nuclear reorganization energy for the semiclassical model was partitioned into  $\lambda_{\text{cl,vib}} = 0.15$  eV,  $\lambda_{\nu} = 0.35$  eV.
- (76) Fajer, J.; Borg, D. C.; Forman, A.; Dolphin, D.; Felton, R. H. *J. Am. Chem. Soc.* **1970**, *92*, 3451.
- (77) Davidson, D. W.; Cole, R. H. *J. Chem. Phys.* **1950**, *18*, 1417.
- (78) Davidson, D. W.; Cole, R. H. *J. Chem. Phys.* **1951**, *19*, 1484.
- (79) Devault, D.; Chance, B. *Biophys. J.* **1966**, *6*, 825.
- (80) Eom, H. S.; Jeoung, S. C.; Kim, D.; Ha, J.-H.; Kim, Y.-R. *J. Phys. Chem. A* **1997**, *101*, 3661.
- (81) Gurzadyan, G. G.; Tran-Thi, T.-H.; Gustavsson, T. *J. Chem. Phys.* **1998**, *108*, 385.
- (82) Akimoto, S.; Yamazaki, T.; Yamazaki, I.; Osuka, A. *Chem. Phys. Lett.* **1999**, *309*, 177.
- (83) Mataga, N.; Shibata, Y.; Chosrowjan, H.; Yoshida, N.; Osuka, A. *J. Phys. Chem. B* **2000**, *104*, 4001.
- (84) Yu, H.-Z.; Baskin, J. S.; Zewail, A. H. *J. Phys. Chem. A* **2002**, *106*, 9845.
- (85) Song, N. W.; Cho, H. S.; Yoon, M.-C.; Jeoung, S. C.; Yoshida, N.; Osuka, A.; Kim, D. *Bull. Chem. Soc. Jpn.* **2002**, *75*, 1023.
- (86) Engleitner, S.; Seel, M.; Zinth, W. *J. Phys. Chem. A* **1999**, *103*, 3013.
- (87) Moser, J. E.; Wolf, M.; Lenzenmann, F.; Grätzel, M. *Z. Phys. Chem.* **1999**, *212*, 85.
- (88) Lenzenmann, F.; Krueger, J.; Burnside, S.; Brooks, K.; Grätzel, M.; Gal, D.; Rühle, S.; Cahen, D. *J. Phys. Chem. B* **2001**, *105*, 6347.
- (89) Zimmermann, C.; Willig, F.; Ramakrishna, S.; Burfeindt, B.; Pettinger, B.; Eichberger, R.; Storck, W. *J. Phys. Chem. B* **2001**, *105*, 9245.
- (90) Shaw, L. E.; Langford, C. H. *Coord. Chem. Rev.* **2002**, *230*, 165.
- (91) Kallioinen, J.; Benkö, G.; Sundström, V.; Korppi-Tommola, J. E. I.; Yartsev, A. P. *J. Phys. Chem. B* **2002**, *106*, 4396.
- (92) Wan, C.; Xia, T.; Becker, H.-C.; Zewail, A. H. *Chem. Phys. Lett.* **2005**, *412*, 158.
- (93) Because the electronic coupling matrix element for ET from the vibrationally unrelaxed  $S_1$  state is expected to depend on excitation energy and time, we considered ET rate constant at 80 K in which the ratio of  $k_{\text{CS}}/k_t$  is maximum to minimize a potential error for the calculation of the electronic coupling matrix element.<sup>86</sup> Note that  $\Delta G_{\text{CS}_2} = \Delta G_{\text{CS}_1} + 0.17$  (eV).